Int J Adv Manuf Technol (2011) 57:245–255
DOI 10.1007/s00170-011-3274-x

ORIGINAL ARTICLE

Adaptive volumetric heat source models for laser beam and laser + pulsed GMAW hybrid welding processes

G. X. Xu · Chuan Song Wu · G. L. Qin · X. Y. Wang · S. Y. Lin

Received: 14 August 2010 / Accepted: 9 March 2011 / Published online: 5 April 2011

Abstract Laser + pulsed gas metal arc welding (GMAW) hybrid welding process is an attractive joining technology in industry due to its synergy of the two processes. It is of great significance to conduct fundamental investigations involving mathematical modeling and understanding of the hybrid welding process. In this study, an adaptive heat source model is first developed for laser beam welding. Through combining the ray-tracing method with the keyhole profile determination technique based on the local energy balance, the keyhole shape and size are calculated and correlated to the distribution parameters of the volumetric heat source model. Then, thermal action characteristics in laser + pulsed GMAW hybrid welding are considered from viewpoint of macro-heat transfer, and a combined volumetric heat source model for hybrid welding is developed to take consideration of heat input from laser, pulsed gas metal arc, and overheated droplets. Numerical analysis of thermal conduction in hybrid welding is conducted. The shape and size of fusion zone and weld dimension in the quasi-steady state are calculated for various hybrid welding conditions, which have a fair agreement with the experimental results.

Keywords Hybrid welding · Keyhole geometry · Numerical analysis · Temperature profile · Weld dimension

G. X. Xu · C. S. Wu (✉) · G. L. Qin
Key Lab for Liquid–Solid Structure Evolution and Materials Processing (Ministry of Education) and Institute of Materials Joining, Shandong University,
Jinan, China
e-mail: wucs@sdu.edu.cn

X. Y. Wang · S. Y. Lin
Harbin Welding Institute, China Academy of Machinery Science and Technology,
Harbin, China

1 Introduction

Since the digital waveform control makes the metal transfer mode run under the condition of one-droplet-per pulse during pulsed gas metal arc welding (GMAW), the welding process is very stable, and there is almost no spatter [1]. However, pulsed GMAW, as a variant of GMAW process, still has shortcomings of lower welding speed, less weld penetration, and wider width of heat-affected zone (HAZ). Though laser beam welding offers deep weld penetration with high welding speed and small HAZ width, it requires stringent parts positioning with lower gap bridging ability and its high welding speed leads to high solidification rates which may in turn lead to cracking and/or pores in the seam [2]. To enhance capability of two processes and compensate deficiencies of each individual, laser + pulsed GMAW hybrid welding process has been developed. Reported advantages of this new process are an increase in (1) the welding speed, (2) the weldable thickness, (3) the gap bridging ability, (4) the weld quality with reduced susceptibility to pores and cracks, as well as (5) the process stability and efficiency. Thus, laser + pulsed GMAW hybrid welding has significant potential of wide applications in manufacturing industry [3–6].

However, for laser + pulsed GMAW hybrid welding process, the number of process parameters is increased because it involves not only the parameters of individual process, but also the new parameters resulting from the combination of two processes, such as the relative position and posture between the laser head and GMAW torch [7]. Though the increased number of process parameters allows a flexible adjustment of the hybrid welding process, it places higher demands on the technology development and the process optimization [8]. Until now, most of the relevant welding parameters are determined empirically, which requires a substantial level of practical experience. There is still a lack of fundamental investigations involving mathematical modeling and understanding of hybrid welding process [8, 9].

In hybrid welding, larger aspect ratio weld is produced by keyhole phenomena. To develop adaptive heat source model for laser + pulsed GMAW hybrid welding process, it is essential to describe the thermal action of laser beam on the workpiece appropriately. To describe the deep penetration weld related to laser welding, three-dimensional volumetric distribution of heat source on the weldment must be taken into consideration. In this study, adaptive combined volumetric heat source models are established to investigate thermal conduction mechanism in laser beam welding and laser + pulsed GMAW hybrid welding processes, respectively. The distribution parameters of the volumetric heat source models are calibrated by the predicted keyhole dimensions. The temperature profiles and weld pool geometry in laser welding and hybrid welding are numerically analyzed. It lays foundation for process optimization and helps to understand the heat transfer mechanism during the hybrid welding process from the viewpoint of engineering.

2 Heat source model for laser beam welding

In laser beam welding, the high intensities of the focused beam lead to the formation of a keyhole in the weld pool. As shown in Fig. 1, the generated keyhole enables the beam to penetrate deep into the workpiece and to distribute the entrained energy over the depth greatly increasing the penetration depth with no appreciable enlargement of the weld seam width. Although several kinds of volumetric heat sources were used to model the laser keyhole welding process [10–14], they all do not fully take into account the complex laser power distribution features in keyhole mode laser welding. In this study, a novel kind of volumetric heat source model in the form of curve-rotated body is established to describe the heat input in keyhole mode laser beam welding.

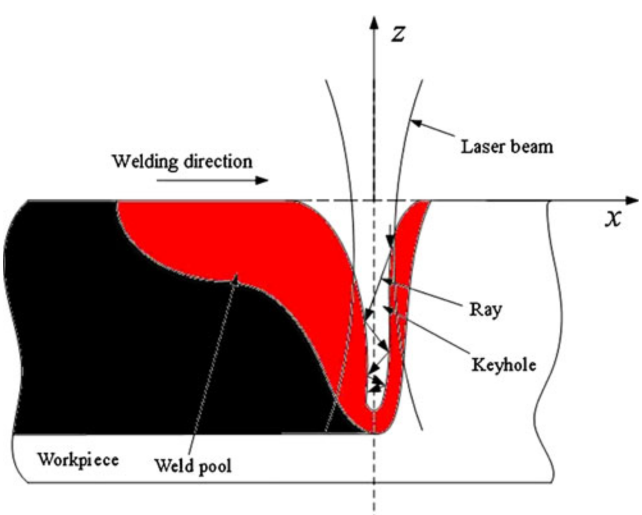

Fig. 1 Schematic of keyhole laser welding

2.1 Rotary volumetric heat source

As demonstrated in Fig. 2, the key features of the proposed volumetric heat source mode are as follows:

1. The heat input from laser beam is distributed within a domain defined by a curve-rotated body. Its height is equal to ($z_e - z_i$), while its radius $r_0(z)$ is tapered from top to bottom surfaces according to a certain rule along the thickness direction of the workpiece. During the laser deep penetration welding, laser energy acts on the workpiece through the keyhole, i.e., laser energy is mainly concentrated inside the keyhole. The radii of heat action domain at the top (r_e) and bottom surfaces (r_i) are determined according to the keyhole geometry.
2. In any plane perpendicular to the central axis (z axis), the heat density distribution within the domain is described by the Gaussian function [15],

$$q_L(r,z) = q_m(0,z)\ \exp\left(-\frac{3r^2}{r_0^2(z)}\right) \qquad (1)$$

   where, $q_L(r, z)$ is the heat flux distribution function, $q_m(0, z)$ is the power density at the central axis, and $r_0(z)$ is the heat distribution parameter.
3. In keyhole mode laser welding, especially for Nd:YAG laser, due to multiple reflection and Fresnel absorption of laser energy on the keyhole wall, the power is concentrated on the lower part of keyhole [15, 16]. So the power density on the bottom of keyhole is much higher. Considering this power distribution feature, the power density $q_m(0, z)$ at the central axis of the heat source increases with a certain rule along the thickness direction of the workpiece. A proportion factor is introduced to describe the difference between the peak power densities at the top ($z=z_e$) and bottom ($z=z_i$) surfaces of the domain,

$$\chi = \frac{q_m(0,z_i)}{q_m(0,z_e)} \quad (\chi \geq 1) \qquad (2)$$

   where, χ is the proportion factor, $q_m(0, z_i)$ and $q_m(0, z_i)$ are the power densities at the central axis of bottom and top surfaces of the domain, respectively. In this study, it assumes that $q_m(0, z)$ changes from $q_m(0, z_e)$ on the top surface to $q_m(0, z_i)$ on the bottom surface in a linear way, i.e.,

$$q_m(0,z) = a_1 z + b_1 \qquad (3)$$

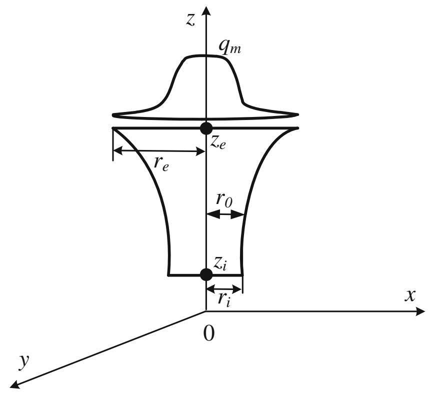

Fig. 2 Schematic of curve-rotated volumetric heat source

Because

$$q_m(0,z_e) = a_1 z_e + b_1, \quad q_m(0,z_i) = \chi q_m(0,z_e) = a_1 z_i + b_1 \tag{4}$$

Then, two coefficients a_1 and b_1 can be obtained by solving the above two equations. And we get

$$q_m(0,z) = q_m(0,z_e)\left(\frac{1-\chi}{z_e - z_i} z + \frac{\chi z_e - z_i}{z_e - z_i}\right) \tag{5}$$

Substituting Eq. 5 into Eq. 1, we obtain

$$q_L(r,z) = q_m(0,z_e)\left(\frac{1-\chi}{z_e - z_i} z + \frac{\chi z_e - z_i}{z_e - z_i}\right) \times \exp\left(-\frac{3r^2}{r_0^2(z)}\right) \tag{6}$$

4. In Eq. 6, different distribution modes are obtained if the radius $r_0(z)$ is tapered from top to bottom surfaces in different functions. The way how $r_0(z)$ varies determines what kind of curve-rotated body takes the heat action domain related to keyhole laser welding. In this study, one kind of tapering function is used, i.e., $r_0(z)$ changes in parabolic curve.
5. The heat source model describing laser beam welding is the repeated addition of a series of heat density functions in Gaussian form with different peak values q_m (0, z_e) and parameters $r_0(z)$. Once the peak value q_m (0, z_e) and the parameter $r_0(z)$ are known, Eq. 6 has specific version, and the heat source model is determined.

Let $r_0(z)$ changes in a parabolic curve,

$$r_0(z) = \frac{z^2}{p} + s \tag{7}$$

Since $r_i = \frac{z_i^2}{p} + s, \;\; r_e = \frac{z_e^2}{p} + s$ Through solving these two equations, we get

$$p = \frac{z_e^2 - z_i^2}{r_e - r_i} \;\; , \;\; s = \frac{r_i z_e^2 - r_e z_i^2}{z_e^2 - z_i^2} \tag{8}$$

$$r_0(z) = \frac{r_e - r_i}{z_e^2 - z_i^2} z^2 + \frac{r_i z_e^2 - r_e z_i^2}{z_e^2 - z_i^2} \tag{9}$$

Integrating the heat density function within the domain, and applying the law of energy conservation,

$$\eta_L Q_L = \int_{z_i}^{z_e}\int_0^{2\pi}\int_0^{r_0(z)} q(r,z) r dr d\theta dz = \int_{z_i}^{z_e}\int_0^{2\pi}\int_0^{r_0(z)} q_m(0,z_e)\left(\frac{1-\chi}{z_e - z_i} z + \frac{\chi z_e - z_i}{z_e - z_i}\right)\exp\left(-\frac{3r^2}{r_0^2(z)}\right) r dr d\theta dz \tag{10}$$

where, η_L is the power efficiency, and Q_L is the laser power. After a series of integration and manipulation, the following expressions are obtained,

$$q_m(0,z_e) = \frac{3\eta_L Q_L}{\pi(1-e^{-3})(E+F)} \tag{11}$$

where two intermediate variables are defined as follows

$$E = \frac{1-\chi}{z_e - z_i}\left[\left(\frac{1}{p^2}\frac{z_e^6}{6} + \frac{s}{p}\frac{z_e^4}{2} + \frac{s^2}{2} z_e^2\right) - \left(\frac{1}{p^2}\frac{z_i^6}{6} + \frac{s}{p}\frac{z_i^4}{2} + \frac{s^2}{2} z_i^2\right)\right] \tag{12}$$

$$F = \frac{\chi z_e - z_i}{z_e - z_i}\left[\left(\frac{1}{p^2}\frac{z_e^5}{5} + 2\frac{s}{p}\frac{z_e^3}{3} + s^2 z_e\right) - \left(\frac{1}{p^2}\frac{z_i^5}{5} + 2\frac{s}{p}\frac{z_i^3}{3} + s^2 z_i\right)\right] \tag{13}$$

Finally, the heat density function for the volumetric heat source can be written as

$$q_L(r,z) = \frac{3\eta_L Q_L}{\pi(1-e^{-3})(E+F)} \times \left(\frac{1-\chi}{z_e - z_i} z + \frac{\chi z_e - z_i}{z_e - z_i}\right)\exp\left(-\frac{3r^2}{r_0^2(z)}\right) \tag{14}$$

where $r_0(z)$ is defined by Eq. 9.

It can be seen that the rotary volumetric heat source is constructed by superimposing a number of Gaussian plane heat sources with different peak power densities and distribution parameters along the thickness direction of the workpiece. The volumetric heat source model here can be determined by the domain dimensions (r_e, r_i, z_e, z_i). How to correlate these domain dimensions (distribution parameters) to the keyhole geometry is introduced next.

2.2 Algorithm for keyhole geometry

Kaplan developed a model to calculate the keyhole profile using a point-by-point determination of the energy balance at the keyhole wall [17]. The corresponding absorbed power transferred to the keyhole wall balances the conduction losses, which yields the local inclination of the wall. As shown in Fig. 3, the geometry of the keyhole wall in the longitudinal section may be calculated point-by-point by locally solving the energy balance at the wall.

As illustrated in Fig. 3a, the local keyhole wall angle θ is determined by the balance between the heat flux conducted into the keyhole wall, q_v, the locally absorbed beam energy flux, I_a, and the evaporation flux, I_{evp}. The heat balance on the keyhole wall requires that following relation is valid

$$\tan(\theta) = \frac{q_v}{I_a - I_{\mathrm{evp}}} \tag{15}$$

The calculation of local keyhole wall angle θ requires the values of q_v, I_a, and I_{evp}. The main advantage of Kaplan's model is simple, but its main shortcoming is the oversimplification for calculating I_a. The locally absorbed beam energy flux I_a on the keyhole wall is calculated by taking into account the Fresnel absorption by the workpiece during multiple reflections and the plasma absorption. The previous models [17, 18] used a conical keyhole to estimate the locally absorbed beam energy flux I_a on the keyhole wall, and did not consider the curvature of the local keyhole wall. In addition, a constant absorption coefficient was used to calculate the value of I_a.

Cho and Na used a ray tracing technique to calculate the multiple reflection and Fresnel absorption [15]. Here, this ray tracing technique is used to determine the locally absorbed beam energy flux I_a on the keyhole wall. Therefore, the ray tracing technique is combined with the point-by-point determination of the energy balance at the keyhole wall.

To implement the multiple reflections in analysis, a ray tracing technique with the discrete grid cell system is proposed as shown in Fig. 4. First of all, a ray vector is formed from the focal point to an arbitrary cell denoted as $\vec{I}$. Some portion of the energy contained in the ray is absorbed according to the Fresnel absorption model, and the rest is delivered by the reflected ray $\vec{R}$ to the point P_r on the opposite side by the following simple vector equation.

$$\vec{R} = \vec{I} + 2\left(-\vec{I}\cdot\vec{N}\right)\vec{N} \tag{16}$$

where, $\vec{N}$ indicates the surface normal at that irradiated point P_i.

The molten surface of workpiece is regarded as specular in this study, and it is reasonable to adopt the Fresnel reflection model [15] which is widely accepted for the decision of material's laser absorption rate. Reflectivity R at the molten surface is mainly dependent on the angle between incident ray and surface normal ϕ. The absorption rate α (ϕ) will be $1-R$.

$$\alpha(\phi) = 1 - \frac{1}{2} \times \left[\frac{1+(1-\varepsilon\cos\phi)^2}{1+(1+\varepsilon\cos\phi)^2} + \frac{\varepsilon^2 - 2\varepsilon\cos\phi + 2\cos^2\phi}{\varepsilon^2 + 2\varepsilon\cos\phi + 2\cos^2\phi}\right] \tag{17}$$

$$\varepsilon^2 = \frac{2\varepsilon_2}{\varepsilon_1 + \left[\varepsilon_1^2 + (\sigma_{\mathrm{st}}/\omega\varepsilon_0)^2\right]^{\frac{1}{2}}}$$

The value of ε is related to the electrical conductance per unit depth of metal, σ_{st}, and ε_1, ε_2 denotes the real part of the dielectric constants of metal and plasma respectively. Additionally, ε_0 indicates the permittivity of a vacuum and ω is one of the laser properties representing the angular frequency.

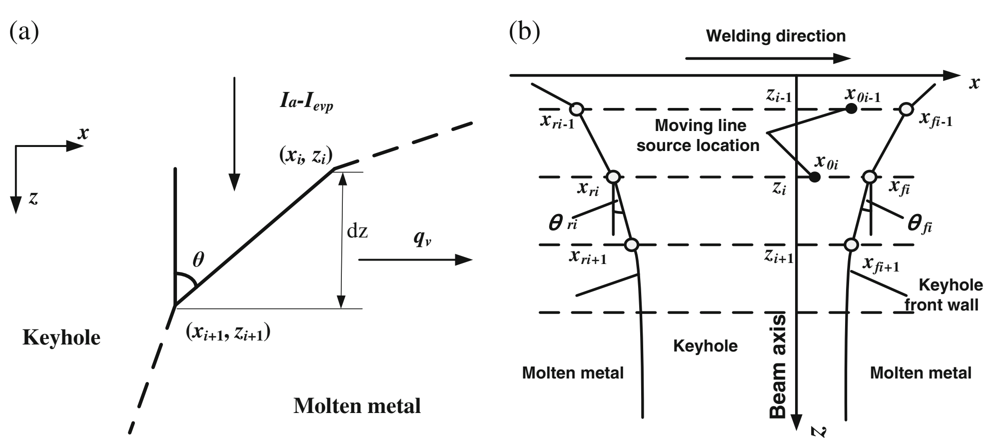

Fig. 3 Schematics of the inclination angle of local keyhole wall and calculation process of keyhole profile [17]

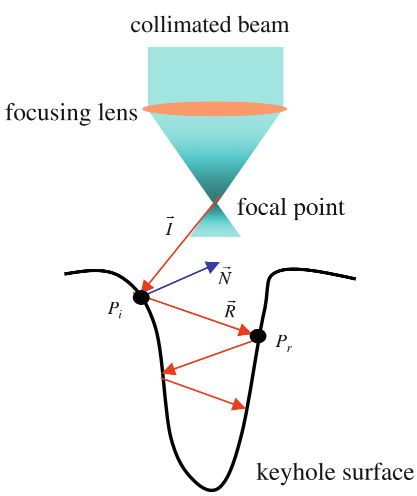

Fig. 4 Schematic diagram of multiple reflection effect in the keyhole [15]

As shown in Fig. 5, a ray is reflected from point P^{k-1} to point P^k, and then to point P^{k+1}. According to geometrical optics approach, the angle α^k between incident ray and reflection ray at point P^k may be written as

$$\alpha^k = \pi - 2\left(\theta_0^k + \theta^k\right) \tag{18}$$

$$\theta_0^k = 2\sum_{n=1}^{k-1} \theta^n \tag{19}$$

where, θ^k is the inclination angle of local keyhole wall at a point where a ray is reflected kth time, and θ^n is the inclination angle of local keyhole wall at a point where a ray is reflected nth time. Since the workpiece is discretized in the thickness direction, it is not possible to find a point to make α^k exactly consistent with the angle between the incident ray and the reflection ray. Therefore, it is necessary to replace it by a point with nearest distance to point P_m^k. And its criterion is expressed as

$$\left|\alpha_m^k - \alpha^k\right| \le \left|\alpha_{m-1}^k - \alpha^k\right| \tag{20}$$

$$\left|\alpha_m^k - \alpha^k\right| \le \left|\alpha_{m+1}^k - \alpha^k\right| \tag{21}$$

where α_{m-1}^k,α_m^k and $\alpha_{m+1}^k$are the angles between incident ray and reflection ray when a ray is reflected to points P_{m-1}^k, P_m^k and P_{m+1}^k, respectively. And α_m^k may be calculated by the following equation

$$\alpha_m^k = \text{arc}\,cos\frac{\left(\overrightarrow{P_m^k} - \overrightarrow{P^k}\right)\cdot\left(\overrightarrow{P^{k-1}} - \overrightarrow{P^k}\right)}{\left|\overrightarrow{P_m^k} - \overrightarrow{P^k}\right|\left|\overrightarrow{P^{k-1}} - \overrightarrow{P^k}\right|} \tag{23}$$

where, $\overrightarrow{P_m^k}$, $\overrightarrow{P^k}$ and $\overrightarrow{P^{k-1}}$ are the vectors of points P_m^k, P^k and P^{k-1}, respectively. α_{m-1}^k and α_{m+1}^k can be calculated in a similar way.

In general, the laser beam absorption is characterized by the Fresnel absorption and the inverse Bremsstrahlung (IB) absorption. The Fresnel absorption is very efficient inside the keyhole due to the multiple reflection of the trapped laser beam. The IB absorption is due to the plasma inside the keyhole which absorbs the laser beam and then redeposits the energy on the keyhole wall by radiation. For Nd:YAG laser, IB absorption plays a minor role [19]. For simplification, the coefficient of IB absorption is still taken as a constant. When a laser beam passes through a plasma of length before hitting the keyhole wall, part of the beam energy is absorbed by the plasma due to IB. For a ray, when it is reflected by mth time to a point on the keyhole wall, its intensity may be written as

$$I_i = e^{-\beta l_m}\prod_{k=1}^{m-1}\left(1-\alpha(\varphi_k)\right)I\left(r_{l,i}, l_1\right) \tag{24}$$

where I_i is the intensity transmitted, β is the IB absorption coefficient, l_m is the total length passing through the plasma when the ray is reflected for mth time, l_1 is the length passing through the plasma when a ray is reflected to the keyhole wall for first time, $r_{l,i}$ is the radial distance from the beam axis to the keyhole wall point hit by a ray for its first time, and α (ϕ_k) is the absorption rate for kth time reflection ($\varphi_k = \alpha^k/2$).

For a point on the keyhole wall, the total absorption energy I_a is the sum of the energy from all direct incident and reflected rays, i.e.,

$$I_a = \sum_{i=1}^{N}\alpha(\phi_m)I_i \tag{25}$$

where, N is the number of rays including the direct incident ray and the coming rays through multiple reflection on the keyhole wall.

Fig. 5 Schematic sketch of the methodology of multiple reflections of laser beam on the keyhole wall

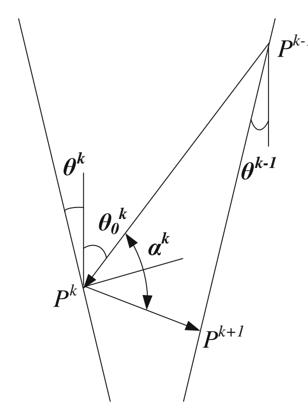

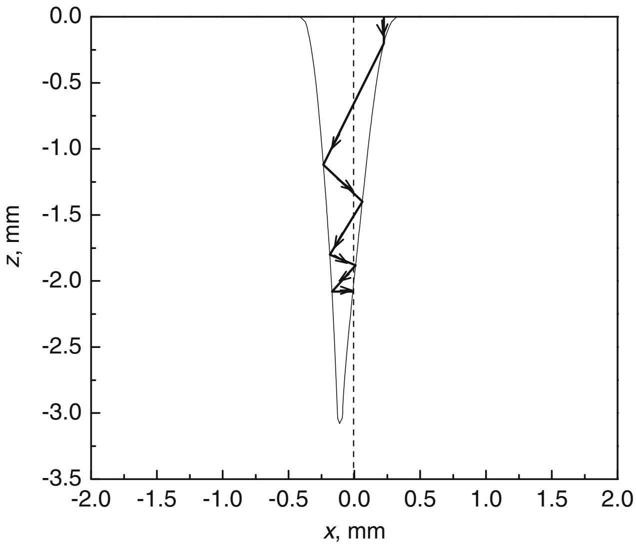

Fig. 6 The calculated keyhole and multiple reflections of a light ray inside the keyhole

The evaporation loss on the keyhole wall is calculated as follows

$$q_{\mathrm{evp}} = m_e L_b \tag{26}$$

where, m_e is evaporation coefficient, and L_b is the latent of evaporation.

The heat losses at each point of the keyhole wall may be expressed as [17]

$$q_v(r,\varphi) = (T_v - T_\infty)\lambda \mathrm{Pe}' \left(\cos\varphi + \frac{K_1(\mathrm{Pe}'\cdot r)}{K_0(\mathrm{Pe}'\cdot r)}\right) \tag{27}$$

To obtain the keyhole profile in the longitudinal cross-section (x–z plane), only the azimuthal angles φ= 0, π are of interest. The heat flow conducted away from the front and rear keyhole wall may be described as

$$q_v(x_f, 0) = (T_v - T_\infty)\lambda \mathrm{Pe}' \left(1 + \frac{K_1(\mathrm{Pe}' x_f)}{K_0(\mathrm{Pe}' x_f)}\right) \tag{27}$$

$$q_v(x_r, \pi) = (T_v - T_\infty)\lambda \mathrm{Pe}' \left(-1 + \frac{K_1(\mathrm{Pe}' x_r)}{K_0(\mathrm{Pe}' x_r)}\right) \tag{28}$$

where r is the radial distance from the local line source to the keyhole wall, x_f, x_y are the distance from the local line source to the front and rear keyhole wall, respectively, T_v, T_∞ are the boiling point and ambient temperature, respectively, λ is the thermal conductivity, K_0 is the modified Bessel function of the second kind and zero order, K_1 is the modified Bessel function of the second kind and first order, and Pe' is a modified Peclet number ($Pe' = v/2a$, v is the welding speed, and a is the thermal diffusivity).

After I_a, q_v, and q_{evp} are known, Eq. 15 can be used to determine the keyhole wall geometry. If a mild steel workpiece of thickness 8 mm is welded with a laser power 2 kW and travel speed 1 m/min, the calculated keyhole geometry and a light ray trace are shown in Fig. 6. It is clear that the ray can reach the bottom of the keyhole after multiple reflections inside the keyhole. Most of the traveling rays in the keyhole are superposed at the keyhole bottom, which results in a deep penetration and an increase in the total energy absorption rate.

2.3 Keyhole-based heat source model for laser welding

When the keyhole geometry is determined, its shape and size are used to calibrate the distribution parameters of the volumetric heat source for laser beam welding.

$$r_e = \frac{x_f - x_r}{2} \tag{29}$$

$$r_i = \frac{r_e}{2} \tag{30}$$

$$z_e - z_i = H_K \tag{31}$$

$$z_e = L$$

where ($x_f - x_r$) is the keyhole length at the top surface, H_K is the keyhole depth, and L is the workpiece thickness. Therefore, the distribution parameters of volumetric heat source for laser beam welding are correlated with the keyhole shape and size.

3 Heat source model for hybrid welding

Based on the appropriate description of heat input from laser beam, pulsed GMAW and heat content of droplets, adaptive heat source model for laser + pulsed GMAW hybrid welding is developed through combining three parts of heat density.

In the pulsed GMAW process, the peak current is usually much greater than the background current and both

Table 1 The process parameters in laser welding (other parameters: focal radius 0.6 mm, focal length 200 mm, beam defocusing −1 mm)

Test No.	Laser power, kW	Welding speed, m/min
1	2.0	1.2
2	2.0	1.8
3	1.8	1.0
4	2.0	1.0

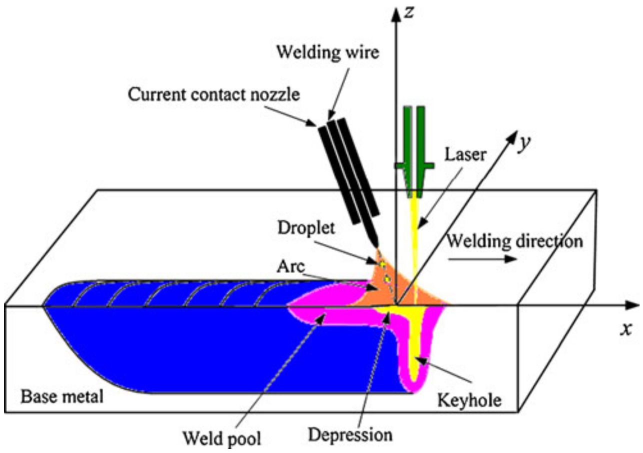

Fig. 7 Schematic of the laser + pulsed GMAW hybrid welding process

alternatively act on the workpiece. One single heat source is not able to reflect the features of pulsed GMAW process. When pulsed GMAW is combined with laser welding, the hybrid welding process is operating at a higher welding speed. If sole pulsed GMAW works at such high speed, its weld penetration is comparatively small. Thus, it is reasonable to treat the heat input of pulsed GMAW arc as two double elliptic heat sources with different distribution parameters, which are corresponding to the average peak and background heat input, respectively.

During pulsed GMAW, the overheated droplets impinge onto weld pool surface with high velocity and carry extra heat content into weld pool. This part of droplet heat has a certain impact on the weld pool geometry. So it is necessary to take into account the droplet heat content in modeling temperature field and weld pool geometry. In addition, droplets deliver momentum into weld pool and result in pool surface depression. Thus, the heat content of overheated droplets should distribute in a region within weld pool. In this

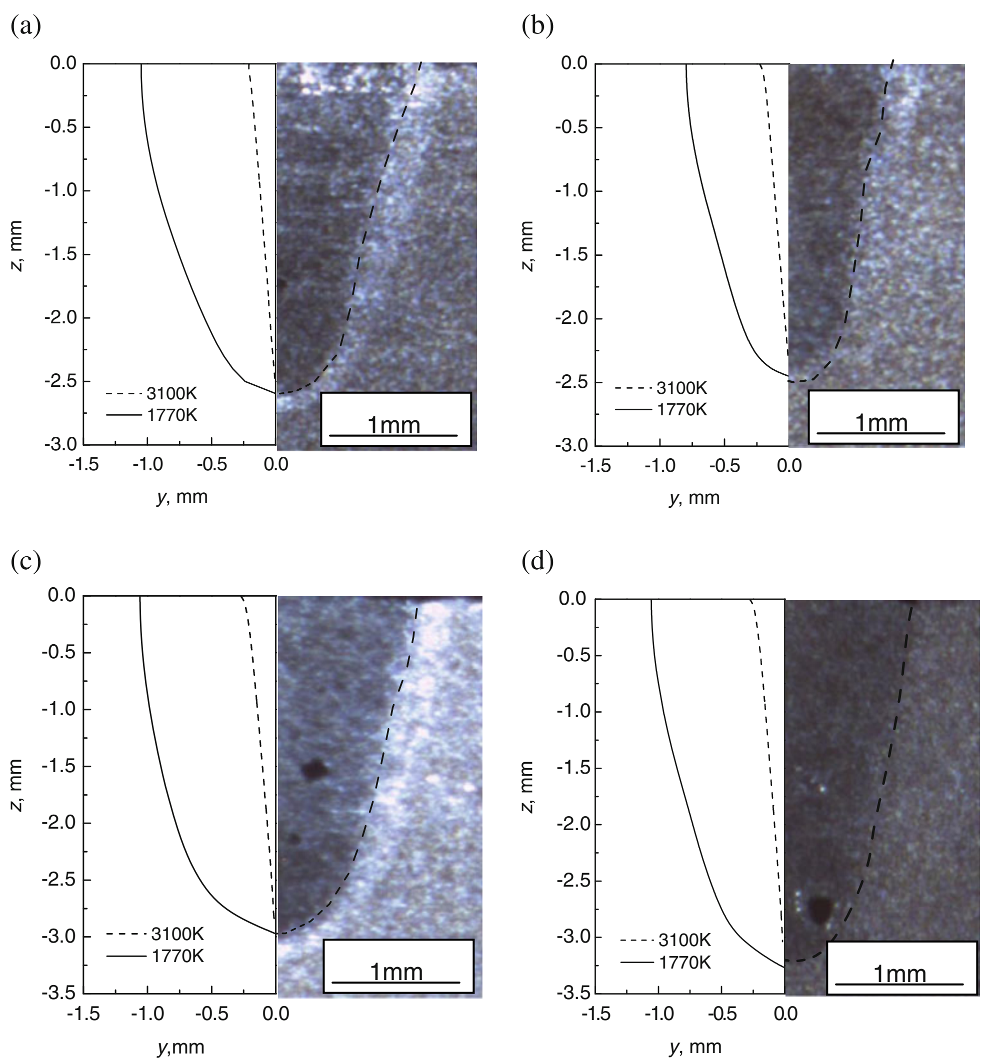

Fig. 8 Comparison between the calculated and measured transverse cross-section geometry of laser welds **a** test 1, **b** test 2, **c** test 3, **d** test 4

Table 2 The process parameters in laser+GMAW-P hybrid welding

Test no.	Base current/A	Peak current/A	Averaged current/A	Averaged voltage/V	Pulse frequency/Hz	Wire feed rate/m min^{-1}
1	15.6	528.0	119.7	22.9	116	4.1
2	15.6	525.0	144.4	24.0	125	5.0

Other parameters are as follows: laser power 2,000 W; welding speed, 1 m/min; wire diameter, 1.2 mm; wire extension, 16 mm; focus position, −1 mm

study, this region is treated as a double ellipsoid within which the relevant heat density is uniformly distributed with time-averaged heat density.

The following three parts of heat input into weldment are combined together, i.e., double elliptic planar distribution of both peak and background duration from pulsed arc, double ellipsoid body distribution of droplet heat content, and parabolic curve-rotated body distribution of laser beam with linearly enhanced peak density along the centerline. To describe this model mathematically, it can be written as

$$q_V(x,y,z) = \left[q_{ap}(x,y) + q_{ab}(x,y)\right] + q_d + q_L(r,z) \quad (32)$$

where $r = \sqrt{x^2 + y^2}$.

4 Results and discussion

First, the keyhole-based heat source model for laser beam welding is used to calculate the temperature field in laser beam welding. The process parameters are listed in Table 1. The material of workpiece is mild steel with thickness of 8 mm. During the calculation process, the keyhole geometry is first calculated, and then the distribution parameters for the volumetric heat source are determined automatically. The proportion factor χ takes a value of 2.0 in this study. Figure 7 shows the comparison between the predicted and measured transverse cross-section of laser weld under different conditions. On the left-hand side, the solid line and dotted line demonstrate the predicted fusion line and keyhole wall, respectively. On the right-hand side is the macro-photograph of laser welds. The calculated keyhole radius at top surface is almost near the focal radius of laser beam, while the keyhole depth is near but slightly less than the weld penetration. The predicted transverse cross-sections of laser welds agree with the experimentally measured ones.

Then, the combined volumetric heat source model is employed to calculate the temperature field in laser + pulsed GMAW hybrid welding. This study is mainly concentrated on the prediction of weld geometry and temperature profiles through developing adaptive heat source model. To speed up the simulation process and focus on main mechanisms in hybrid welding, only the heat conduction problem in the quasi-steady state is considered, and the fluid flow in the weld pool is not dealt with at this stage.

As shown in Fig. 8, the coordinates system is moving at the welding speed along the welding direction (x-axis), z-axis along the opposite thickness direction and the origin coincident with intersection point between top surface of the workpiece and the arc centerline for hybrid welding.

Hybrid welding was conducted on mild steel workpiece of 8-mm thickness. As shown in Fig. 8, laser beam was leading and the arc was trailing. The laser beam was perpendicular to the top surface of workpiece, while the axis of GMAW torch was 27^0 titled with respect to the centerline of laser beam. The laser-arc distance was 1.0 mm. The shielding gas was Ar+18%CO_2. The mode of metal transfer was one droplet for each pulse. The process parameters are listed in Table 2. The combined volumetric heat source model for hybrid welding is used to calculate the temperature profile.

Figure 9 shows the calculated and measured weld cross-section of laser + pulsed GMAW hybrid welding for test 1. The previous mode [5, 6] is that the distribution parameters of volumetric heat source are selected according to experimental data and expertise, while the new mode in this study is that the distribution parameters of volumetric heat source are correlated to the predicted keyhole shape

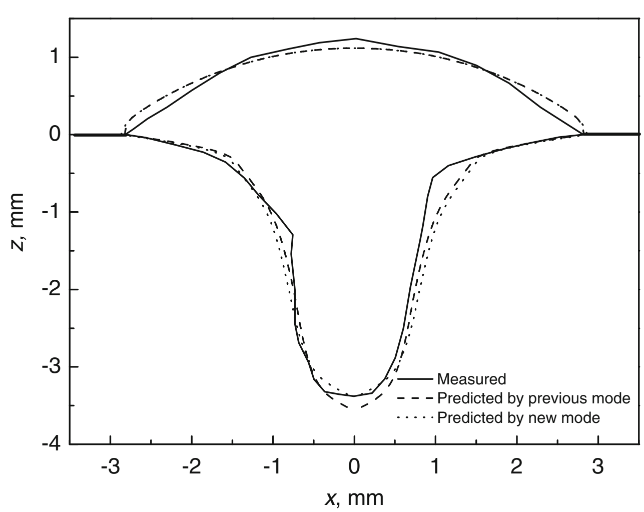

Fig. 9 Comparison of the calculated and measured weld cross-section in hybrid welding (test 1)

Fig. 10 The predicted weld geometry (**a**) and temperature fields (**b**–**f**) in hybrid welding (test 2)

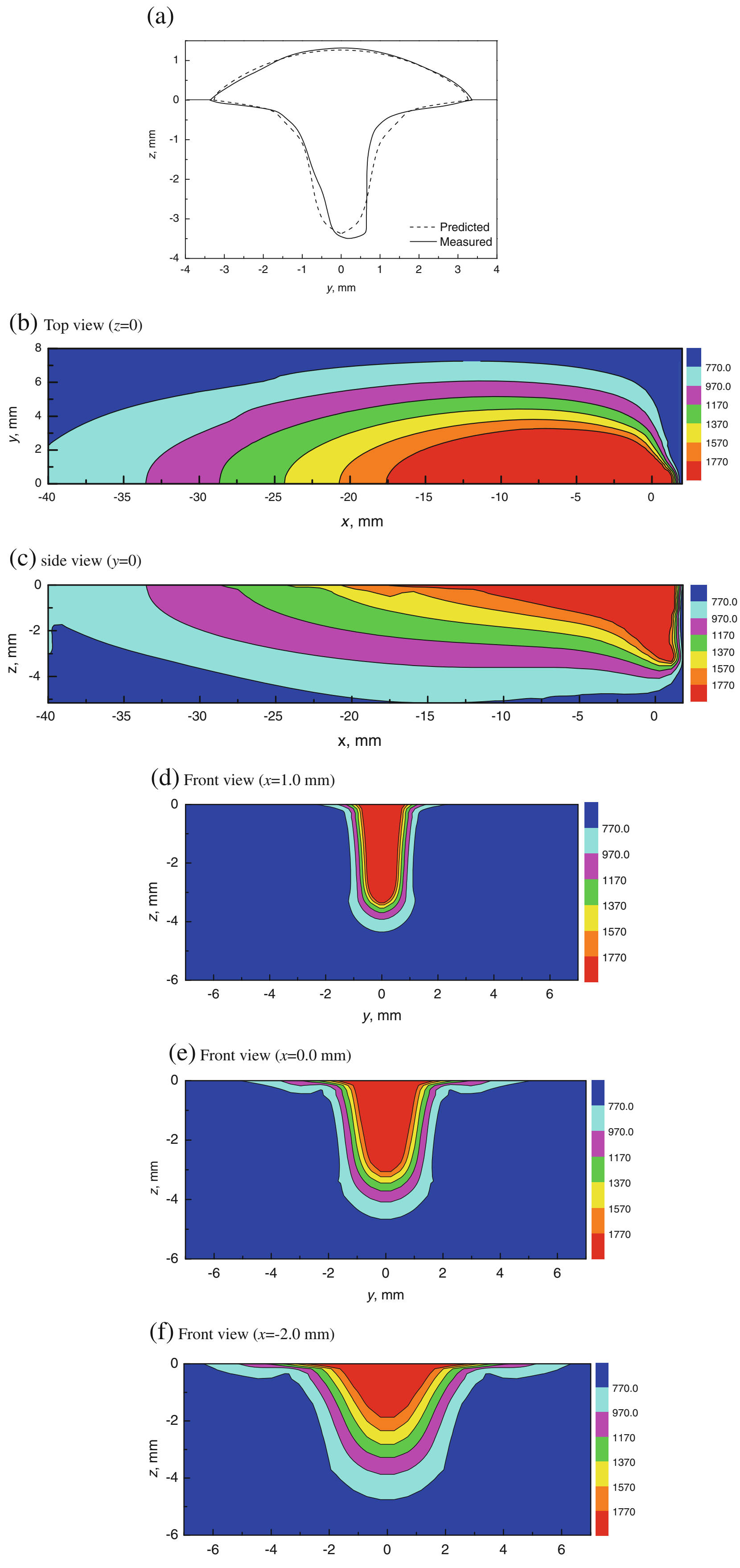

and size. It is seen that the predicted and experimental results are in good agreement, and the calculation accuracy is improved by using the new mode. It demonstrates that the new heat source model is suitable to simulate the laser + pulsed GMAW hybrid welding process effectively.

Figure 10a compares the predicted weld cross-section of hybrid welding with the measured one for test 2, while Figs.10b–f demonstrate the predicted temperature fields at different positions. The weld pool boundary is represented by the 1745 K solidus isotherm. Figure 10b and c are the temperature profiles at top surface and longitudinal cross-section of workpiece, respectively. Figure 10d is the temperature field at transverse cross-section at $x=1$ mm. As shown in Fig. 8, this location is the axis of laser beam, so the fusion zone with larger depth–width ratio is dominated by laser power. The location $x=0$ is between the laser beam and the GMAW torch, so that Fig. 10e shows a fusion zone resulted from the combined effect of both laser beam and arc power. Figure 10f illustrates a fusion zone behind the arc ($x=-2.0$ mm), thus, it is just affected by the arc power.

5 Conclusions

1. To depict characteristics of heat source action in laser deep penetration welding, one new kind of heat density distribution mode is proposed. The heat source model describing laser beam welding is the repeated addition of a series of heat density functions in Gaussian form with different peak values and distribution parameters within a curve-rotated body, while its volume radius is tapered from top to bottom surfaces according to parabolic curve, and its power density at the central axis of the heat source increases linearly along the thickness direction of the workpiece, respectively.
2. The ray tracing technique is combined with the Kaplan's method for determining keyhole profile using a line heat source and local energy balance at keyhole wall. The multiple reflections of laser rays inside the unsymmetrical keyhole and Fresnel absorption of laser energy by keyhole wall are calculated. The prediction accuracy of keyhole shape and size is improved. The calculated keyhole dimensions are correlated with the distribution parameters of the volumetric heat source for laser welding. Based on the developed heat source model for laser beam welding, the predicted transverse cross-sections of laser weld are in good agreement with the experimental measured ones.
3. Based on the appropriate description of heat input from laser beam, pulsed GMAW and heat content of droplets, the combined heat source model is developed for laser + pulsed GMAW hybrid welding through combining three parts of heat density. The developed adaptive volumetric heat source model is employed to conduct numerical analysis of temperature fields and weld dimensions in laser + pulsed GMAW hybrid welding. The experimental results show that the computed transverse cross-sections of hybrid welds match well with the measured values for various welding conditions.

Acknowledgments The authors are grateful to the National Key Technologies R&D Program of China under Grant No.2006BAF04B10 and the National Natural Science Foundation of China under Grant No.51074098 for the financial support for this research.

References

1. Matsuyama K (2003) Digital control used in welding machines. In: Chinese Mechanical Engineering Society (ed) Proceedings of International Forum on Welding Technology in Automobile Industry, Beijing, China, pp 81–87
2. Rasmussen D, Dubourg L (2006) Hybrid laser-GMAW welding of aluminium alloys: a review. In: David SA, DebRoy, T (eds). Proceedings of 7th International Conference on Trends in Welding Research, Pine Mountain, USA, pp. 133–142
3. Staufer H (2007) Laser hybrid welding in the automobile industry. Weld J 86(10):36–40
4. Defalco J (2007) Practical applications for hybrid laser welding. Weld J 86(10):47–50
5. Xu GX, Wu CS, Qin GL, Wang XY, Lin YS (2008) Numerical simulation of weld formation in laser+GMAW hybrid welding II. Combined volumetric distribution mode of hybrid welding heat source. Acta Metall Sinica 44:641–646
6. Xu GX, Wu CS, Qin GL, Wang XY, Lin YS (2009) Numerical simulation of weld formation in laser+GMAW hybrid welding III. Treatment of pulsed arc action and improvement of heat source modes. Acta Metall Sinica 45:107–112
7. Shi S, Howse D (2007) Laser welding and laser-MAG hybrid welding of structure steels in shipyard. In: Chinese Mechanical Engineering Society (Ed.), Proceedings of International Forum on Welding Technology in Shipbuilding Industry, Beijing, China, pp.41–53
8. Mahrle A, Beyer E (2006) Hybrid laser beam welding—classification, characteristics, and applications. J Laser Appl 18:169–180
9. Bagger C, Olsen FO (2005) Review of laser hybrid welding. J Laser Appl 17:2–14
10. Goldak J, Chakravarti A, Bibby M (1984) A new finite element model for welding heat sources. Metall Trans B 15:229–305
11. Sabapathy PN, Wahab MA, Painter MJ (2001) Numerical methods to predict failure during the in-service welding of gas pipelines. J Strain Anal Eng Des 36:611–619
12. Wu S, Zhao HY, Wang Y, Zhang XH (2004) A new heat source model in numerical simulation of high energy beam welding. Trans China Weld Inst 25:91–94
13. Goldak J, Bibby M, Moore J (1986) Computer modeling of heat flow in welds. Metall Trans B 17:587–600
14. Sonti N, Amateau MF (1989) Finite-element modeling of heat flow in deep-penetration laser welds in aluminum alloys. Numer Heat Transfer A 16:351–378
15. Cho JH, Na SJ (2006) Implementation of real-time multiple reflection and Fresnel absorption of laser beam in keyhole. J Phys D Appl Phys 39:5372–5378

16. Tu JF, Inoue T, Miyamoto I (2003) Quantitative characterization of keyhole absorption mechanisms in 20 kW class CO2 laser welding processes. J Phys D Appl Phys 36:192–203
17. Kaplan A (1994) A model of deep penetration alser welding based on calculation of the keyhole profile. J Phys D Appl Phys 27:1805–1814
18. Zhao H, DebRoy T (2003) Macroporosity free aluminum alloy weldments through numerical simulation of keyhole mode laser welding. J Appl Phys 93:10089
19. Rai R, Elmer JW, Palmer TA, DebRoy T (2007) Heat transfer and fluid flow during keyhole mode laser welding of tantalum, Ti-6Al-4V, 304 stainless steel and vanadium. J Phys D Appl Phys 40:5753–5766